Intraoperative Impedance-Based Estimation of Cochlear Implant Electrode Array Insertion Depth

Philipp Aebischer , Stefan Meyer, Marco Caversaccio , and Wilhelm Wimmer

Abstract—*Objective:* **Cochlear implant impedances are influenced by the intracochlear position of the electrodes. Herein, we present an intuitive approach to calculate tissue resistances from transimpedance recordings, ultimately enabling to estimate the insertion depth of cochlear implant electrodes.** *Methods:* **Electrode positions were measured in computed-tomography images of 20 subjects implanted with the same lateral wall cochlear implant model. The tissue resistances were estimated from intraoperative telemetry data using bivariate spline extrapolation from the transimpedance recordings. Using a phenomenological model, the electrode insertion depths were estimated.** *Results:* **The proposed method enabled the linear insertion depth of all electrodes to be estimated with an average error of 0.76 ± 0.53 mm.** *Conclusion:* **Intraoperative telemetry recordings correlate with the linear and angular depth of electrode insertion, enabling estimations with an accuracy that can be useful for clinical applications.** *Significance:* **The proposed method can be used to objectively assess surgical outcomes during and after cochlear implantation based on non-invasive and readily available telemetry recordings.**

Index Terms—**Biomedical measurement, telemetry, deafness, ear, electrodes, impedance, impedance measurement.**

I. INTRODUCTION

COCHLEAR implants have become a successful treatment for severe-to-profound hearing loss [1]. A crucial part of the implantation is the insertion of the electrode array into the scala tympani. The impact of the angular insertion depth of the electrode array on hearing outcomes is a much-debated topic [2]. However, there is common agreement that objective measures on electrode placement are beneficial to assess surgical outcome and may help in the implant fitting procedure [3]–[6].

Electrode placement can be assessed using medical imaging (e.g. computer tomography) [7]. This allows to accurately localize the electrodes, but imposes additional radiation risk on the patient, is time consuming and thus rarely done intraoperatively. On the other hand, implant telemetry is typically recorded intraoperatively. It is commonly used to verify implant integrity, as high impedances can be indicative of open circuits (e.g. extracochlear placement or implant malfunction [8]).

In addition to the overall electrode impedances, all modern cochlear implants can be used to record a voltage matrix $\mathbf{V}$ [3], whose elements $v_{i,j}$ represent the measured voltage potential at the jth electrode when stimulating electrode i. The diagonal elements of the voltage matrix can be understood as the voltages that cause currents of a predefined value I_{stim} through the corresponding electrodes and are related to the electrode impedances by Ohm's law. Some authors refer to this recording as transimpedance measurements (TM) [9], impedance and field telemetry (IFT) [10] or electric field imaging (EFI) [11], although the latter term can be misleading, as the process does not capture any geometrical information.

Vanpoucke *et al.* showed that transimpedance measurements are predictive of tip fold-over [12], also later confirmed by Zuniga *et al.* [13]. Tan *et al.* found that impedances change with electrode position during real-time measurements in cadaveric electrode insertions as well as in vivo implantation [14]. This dependency was confirmed by Giardina *et al.* in a plastic cochlear model, who also showed a correlation with perimodiolar distance [15]. However, Tan *et al.* did not attempt to directly predict electrode position from impedance measurements, while Giardina *et al.* limited their analysis to a single 3d-printed cochlear analogon, which excludes patient-specific differences in anatomy and can not fully reproduce in-vivo current flow as "the plastic model afforded no "leaky" transverse channels" [15].

The goal of this study was to systematically investigate and determine the relation between intraoperatively recorded clinical telemetry data and linear and angular electrode positions. We hypothesize that impedances correlate with linear and angular insertion depths and that this correlation enables to estimate the insertion depth of electrode contacts from clinical impedance recordings.

As these recordings are routinely performed for implant verification, such a method could potentially contribute to assessing the surgical outcome directly after implantation without the need

for medical imaging. The presented work aims to overcome limitations of previous work on this subject, that did not take into account exact geometric positions of the electrode contacts [14] or was performed in vitro [15].

II. MATERIALS AND METHODS

A. Study Design and Population

The study was approved by our local institutional review board (Cantonal Ethics Committee Bern, No. 165/11). Written informed consent for participation in the study was obtained before undergoing the study procedure. 20 adults subject to cochlear implantation participated in the study (aged 20 years to 88 years, average 51 years, 8 male 12 female, 10 left and 10 right ears). Only subjects receiving the same implant type (Synchrony + $Flex^{28}$ array, Med-El, Austria) were included to ensure homogeneity by identical electrode array geometry covering deep insertions. The collected data consisted of pre- and postoperative computed tomography (CT) or cone beam CT images and intraoperative telemetry recordings.

B. Implant Telemetry

All patients were implanted with a transmastoid posterior tympanotomy approach using a round window access. After insertion of the electrode, the round window niche was sealed with fat tissue. The wound was temporarily closed and implant telemetry recorded using the manufacturer's telemetry software (Maestro, Med-El), according to the clinical standard procedure at our institution. To avoid movement during the recording, care was taken to omit contact with the patient and operating table.

The recorded telemetry corresponds to the routinely performed implant integrity test. We did not carry out any additional measurements nor were any recording settings changed from the implant test protocol specified by the manufacturer. The implants perform telemetry measurements with charge balanced, rectangular biphasic cathodic-first pulses with an amplitude of $I_{stim} \approx 300\ \mu m$ and a pulse-width of 24 μs [16]. The voltage potential on the recording electrode is measured at the end of the anodic phase [17] with respect to a large ground electrode located on the implant body. A schematic drawing of the current stimulus and resulting voltage on the electrode is shown in Fig. 1 (top). The voltage is amplified and digitized by the implant with a resolution of approximately 20 mV, transmitted to the receiver and stored for later processing.

C. Computed-Tomography Imaging

Postoperative imaging was performed either directly after surgery using a mobile cone beam CT scanner ($0.156 \times 0.156 \times 0.2\ mm^3$; xCAT ENT, Xoran Technologies, Ann Arbor MI, USA and ProMax, Planmeca, Helsinki, Finland) or one day after implantation using a CT scanner (voxel size from 0.2 mm to 0.4 mm isotropic; SOMATOM Definition Edge, Siemens, München, Germany.)

D. Electrode Localization and Insertion Depth

The implanted electrode arrays have $N = 12$ separate channels that correspond to 12 evenly spaced locations along an
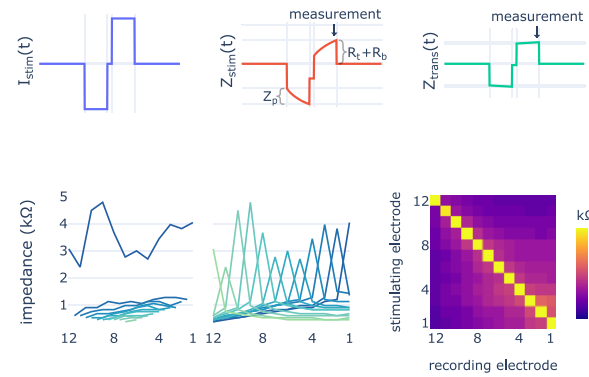

Fig. 1. Top: Schematic drawings of the current stimulus (left), impedance of the stimulating channel (center) and impedance of a non-stimulating channel (right). Bottom: Three different representations of the impedance matrix of subject 4. Left: Diagonal elements (the clinical impedances) and off-diagonal elements (basal direction). Center: Rows of the impedance matrix, related via Ohm's law to intracochlear voltages along the array by the stimulation current $I_{stim} \approx 300\ \mu m$. Right: Pseudocolor plot of the impedance matrix.

Fig. 2. The $Flex^{28}$ electrode array in two orientations (top) and photomicrographs of a single (bottom left) and double (bottom right) contact pads with highlighted outline.

active length of $l = 23.1\ mm$ [10]. The channels are numbered in ascending order from apical (electrode 1) to basal (electrode 12). Seven basal channels end in two electrically connected platinum contact pads on opposite sides of the array, while the remaining five apical channels are connected to single contact pads. As a single basal channel ends in two separate, but electrically connected pads, the exposed surface of each basal pad is halved. This way, the effective surface area is the same for all channels. Images of an electrode array are shown in Fig. 2. A large reference electrode, in respect to which all voltage measurements are performed, is located on the implant body.

For further data processing, a local coordinate system was defined as proposed by Verbist et al. [18]. To reduce uncertainty caused by landmark based modiolus identification, a robust cochlear axis detection algorithm was used [19]. Pre- and postoperative CT images were first cropped, then registered using a normalized mutual information algorithm. Positions of the round window and all electrodes were manually determined in a medical visualization software (Amira, FEI, Burlington, MA)
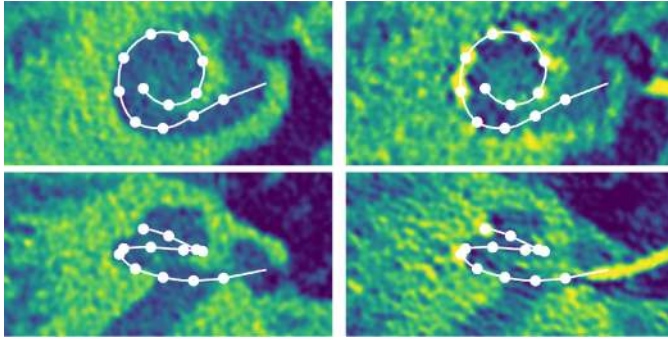
Fig. 3. Cross-sectional images of preoperative (left) and postoperative (right) CT images through the basal and a vertical plane for subject 13. Projections of electrode-positions and the interpolated spline starting at the round window are superimposed on the images.
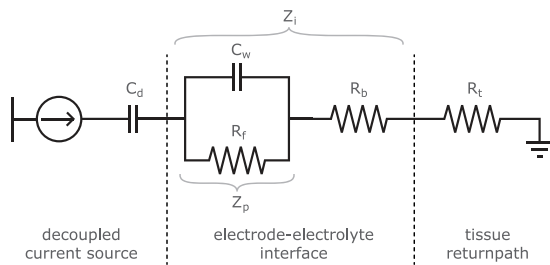

Fig. 4. Equivalent circuit model for a stimulating channel. C_d decouples the implant's current source to prevent non-zero DC charge injection. The electrode-electrolyte interface consists of the Warburg capacitance C_w modelling the electrochemical double layer at the electrode surface, the Faradaic resistance R_f modelling the charge transfer from metal to fluid and a local bulk resistance R_b modelling ohmic resistances in the near-field of the electrode. The tissue resistance R_t models the return path from the electrode site to the ground electrode through biological tissue [11].

and expressed in the local coordinate system by an expert fully blinded to the impedance modelling. The angular insertion depth was computed as the azimuth coordinate in the local cylindrical coordinate system. The linear insertion depth was computed as the length of a quadratic spline starting at the round window and passing through all intermediate electrodes. An example of pre- and postoperative CT images with superimposed electrode positions is shown in Fig. 3.

E. Cochlear Current Paths

A simple electrically equivalent circuit model of a single channel, as proposed by Vanpoucke *et al.* [11] is shown in Fig. 4. In monopolar stimulation mode, the charge is presented at a single contact of the electrode array, where a transition from metallic to ionic charge transport occurs into the perilymph. This transition is commonly characterized with the polarization impedance Z_p [15], [20]. Together with a local bulk resistance R_b, this models the electrode-electrolyte interface. Contributions to R_b can arise from high current density in the vicinity of the electrode, leading to a local potential rise [11] and from air bubbles on the electrodes [8].

As the implant records clinical impedances at the end of a charge-balanced current pulse, the capacitance C_w is in a discharged state. Therefore, the polarization impedance Z_p ideally does not contribute to the measurement. Note that this differs from the impedance measurements of other manufacturers, where the recording is performed in the polarized state of the electrode [21]–[23].

The return path to the implant's ground electrode leads through diverse biological tissues, with conductivities ranging between $1.4 \, \mathrm{S/m^{-1}}$ to $1.8 \, \mathrm{S/m^{-1}}$ for perilymph, $4 \, \mathrm{S/cm^{-1}}$ for nerve tissue and about $2 \, \mathrm{S/cm^{-1}}$ for bone [9], [24], [25]. Different definitions are used for this bulk resistance. Some authors combine the near-field resistance R_b and far-field resistance R_t into the access resistance [9], [15], [20]. Herein, we refer to the far-field component as the tissue resistance R_t, and allow for a resistive component R_b in the interface impedance, adopting the notation of Vanpoucke *et al.* [11]. Finally, the overall electrode impedance

$$Z_e = Z_i + R_t \tag{1}$$

is usually denoted clinical impedance, electrode impedance or simply impedance [14], [15], [20].

The system can be understood as a voltage divider, where the local potential at the electrode site in the perilymph V_{loc} is determined by the ratio of tissue resistance and interface impedance

$$V_{\mathrm{loc}} = V_{\mathrm{rec}} \frac{R_t}{R_t + Z_i}. \tag{2}$$

As both impedances can be expected to be in the same order of magnitude [11], [20], the local potential differs significantly from the recorded voltage V_{rec}. In contrast, the measuring circuit is designed to have a high input impedance, resulting in low current flowing back into the recording electrode. Therefore, transimpedance measurements do correspond to the local potential of non-stimulating electrodes [9], [11], [26].

F. Tissue Resistance Estimation

Interpolating the diagonal elements of the voltage matrix from off-diagonal elements allows to reconstruct the intracochlear potential at the stimulation site, as the influence of the interface impedance on intracochlear potential measurements on non-stimulating electrodes is negligible.

With this estimation of the tissue resistance R_t, one can obtain the interface impedance Z_i using the relation with the clinical resistance (1). Different methods have been suggested to obtain these values. Van den Honert and Kelsall used linear extrapolation from neighboring elements of the voltage matrix [26]. For all but the first and last electrode, there are four directions from which the extrapolation can be approached, and the on-diagonal elements were estimated as the maximum of these four values.

Vanpoucke *et al.* modelled the system as a lumped-element network that represents longitudinal resistors between each electrode and transverse resistors from each electrode to ground [27]. This allows to construct a voltage matrix of the network.

Minimizing the differences of its off-diagonal elements to the measured voltage matrix yields an estimate of the diagonal matrix elements.

In our dataset, all transimpedance values are below 2 kΩ, with a quantization step-size between 61 Ω and 82 Ω. This leads to a coarse representation of the measured data. Extrapolation from a small set of points as used by Van den Honert and Kelsall amplifies errors from the signal quantization. On the other hand, a network with only few knots and edges as described by Vanpoucke *et al.* may be too restrictive to fully describe the complex current flow and voltage distribution in the inner ear.

G. Bivariate Spline Interpolation

We therefore suggest a simple method for extrapolating the diagonal elements by separately fitting a bivariate cubic spline to the upper and lower triangle of the impedance matrix $\mathbf{Z}$. For this purpose, we construct a new matrix

$$
\mathbf{U} = \begin{pmatrix}
z_{1,1} & z_{1,2} & \cdots & \cdots & \cdots & z_{1,12} \\
z_{2,2} & z_{2,3} & \cdots & \cdots & z_{2,12} & z_{2,12} \\
\vdots & \vdots & & \mathinner{\mkern1mu\raise1pt\hbox{.}\mkern2mu\raise4pt\hbox{.}\mkern2mu\raise7pt\hbox{.}} & & \vdots \\
z_{9,9} & z_{9,10} & z_{9,11} & z_{9,12} & \cdots & z_{9,12}
\end{pmatrix}. \tag{3}
$$

The rows of this matrix correspond to the stimulation site, while the columns correspond to the distance between stimulating and recording electrodes in basal direction. Values outside the extent of the array are padded with the value of the last element and the last three rows are omitted, as they contain not much information. The first column carries the clinical impedances and extrapolation of the elements $u_{i,1}$ gives an estimation of the ith tissue resistance.

This extrapolation can be repeated for decays in apical direction, by reversing the ordering of the impedance matrix $\mathbf{Z}$ before constructing the decay matrix $\mathbf{U}$. As with the extrapolation from neighboring elements proposed by Van den Honert and Kelsall [26], this gives a total four directions from where the extrapolation can be approached, leading to two estimations for the three basal and apical and four estimations for the central electrode contacts, from which we compute the mean of each element as our final estimation.

The reason for the proposed rearrangement is that the voltage profile along the array is not smooth, but has a cusp at the location of the stimulation [27]. Interpolating this profile with a smooth function will likely underestimate the real value at the stimulating position. Working on only one triangle of the matrix at a time results in a process better suited for bivariate spline interpolation due to the removal of the cusp. In addition, the two axes of a bivariate function fitted to the matrix run along edges of the interpolating grid. Using fewer knots than the number of electrodes and minimizing the least squares distances of the spline to the impedance matrix allows some smoothing of the quantization noise. For the following analysis, we used twelve knots along the electrodes and four knots along the voltage decay direction.
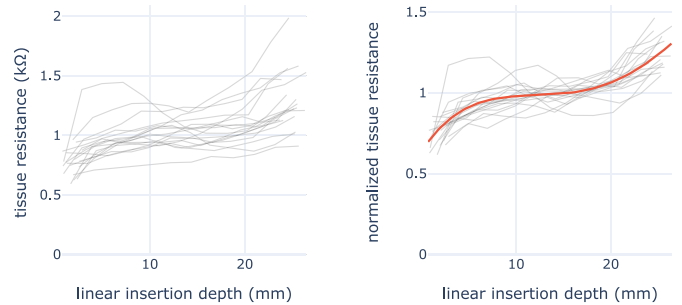

Fig. 5. Tissue resistances (left) computed from bivariate spline extrapolation of transimpedance measurements. A least squares fitted fourth degree polynomial is overlaid on the normalized tissue resistances (right).

H. Estimating Linear Insertion Depth

The tissue resistances computed for all patients using the above method are shown versus the linear insertion depth, computed from CT-data, according to Section II-D, in Fig. 5 (left). In addition to increasing values for deeper electrodes, resistances vary significantly in-between subjects. This is to be expected due to variations in anatomy and length of the return path. However, this second variation can be reduced for further analysis, by working with the normalized tissue resistance

$$
r_t^i = R_t^i / \left(\frac{1}{N} \sum_{k=1}^{N} R_t^k \right), \tag{4}
$$

where the superscript denotes the electrode number. The normalized tissue resistances are shown in Fig. 5 (right), where the correlation with the insertion depth is enhanced. This enables to estimate the insertion depth using a purely phenomenological model.

For a group of subjects $S = \{S_1, \ldots, S_m\}$, the relation between the normalized tissue resistances r_a^i determined from telemetry data and corresponding insertion depths d_i determined from CT-images can be approximated by least squares fitting a polynomial P of coefficients $a_1, \ldots, a_k$,

$$
\min_{a_1,\ldots,a_k} \sum_{S} \sum_{i=1}^{N} \left(r_a^i - P_{a_1,\ldots,a_k}(d_i) \right)^2. \tag{5}
$$

A polynomial of degree 4 is superimposed in Fig. 5 (right). This enables to estimate the insertion depths of all contacts of an additional subject not in group S, without the use of imaging data, by determining the values $\hat{d}_i$ that solve $r_a^i = P_{a_1,\ldots,a_k}(\hat{d}_i)$. In the following, we denote values estimated from telemetry recordings with a hat. In contrast, corresponding parameters without hat refer to values obtained from the imaging data, according to Section II-D.

As the inter-electrode distance Δd is determined by array geometry, the insertion depth of the ith electrode, $\hat{d}_i$, can be obtained from the insertion depth of the basal-most electrode $\hat{d}_N$

$$
\hat{d}_i = \hat{d}_N + (N - i)\Delta d. \tag{6}
$$

This allows to simultaneously estimate insertion depths of all electrode contacts without the need for the subjects imaging data

and with a single parameter $\hat{d}_N$, by minimizing

$$\min_{\hat{d}_N} \sum_{i=1}^{N} \left(r_a^i - P\left(\hat{d}_N + (N-i)\Delta d \right) \right)^2. \qquad (7)$$

For partially inserted electrodes, extracochlear channels should not be included in the estimation process, as the polynomial P only samples the intracochlear space. In this case the normalization of the tissue resistances (4) will not give meaningful results. This can be circumvented by replacing the normalization constant by an additional minimization parameter in (7).

I. Converting Linear to Angular Insertion Depths

From a clinical perspective, it would be particularly interesting to estimate the angular insertion depth of the electrodes. The proposed method, however, is not directly applicable to this task, as the analog of the inter-electrode distance in angular coordinates becomes a function of the position of the electrode array itself and thus of the individual cochlear anatomy. However, there is a strong correlation between linear and angular insertion depths [28]–[30]. Therefore, approximating this relation with a polynomial provides a way to transform linear to angular insertion depths.

The present data shows a Spearman correlation coefficient of $r = 0.994$ ($p < 0.001$). As linear insertion depths have been verified to scale linearly with the cochlear size [29], [30], the estimation can be improved by multiplying the angular insertion depths by the cochlear base length, defined by the length of the line passing from the center of the round window through the cochlear axis to the lateral wall [29], [30]. This enhances the correlation (Spearman's $r = 0.996$, $p < 0.001$).

The estimation can be expressed by determining the polynomial Q, that minimizes

$$\min_{b_1, \ldots, b_j} \sum_{S} \sum_{i=1}^{N} \left(\theta_i \cdot a - Q_{b_1, \ldots, b_j}(d_i) \right)^2, \qquad (8)$$

with the angular depth of the ith electrode θ_i, and the cochlear base length a. Finally, the angular depth can be estimated from the linear depth estimation using $\hat{\theta}_i = Q(\hat{d}_i)/a$ [28]–[30].

J. Lumped-Element Model

Additional insight might be gained by modelling the system as a network of discrete resistive elements, as proposed by Vanpoucke *et al.* [11]. The impedance matrix $\mathbf{Z}_N$ of such a network can be constructed as

$$\mathbf{Z}_N = (\mathbf{A}\mathbf{Y}\mathbf{A}^\intercal)^{-1}, \qquad (9)$$

with the incidence matrix $\mathbf{A}$ describing the topology of the network and the diagonal admittance matrix $\mathbf{Y} = \mathrm{diag}(\boldsymbol{r}_{\mathrm{sol}})^{-1}$ carrying the reciprocal resistances of the node links. A first order network corresponds to N electrodes connected to its neighbors with longitudinal resistors and to ground with transverse resistors. Higher order networks can be constructed by adding additional resistive connections between non-neighboring electrodes.

It is often more intuitive to think in terms of currents along the network edges instead of their resistances. Using Ohm's law, we can compute the voltages on each node

$$\boldsymbol{v}_N = \mathbf{Z}_N \cdot \boldsymbol{i}_N = (\mathbf{A}\mathbf{Y}\mathbf{A}^\intercal)^{-1} \cdot \boldsymbol{i}_N, \qquad (10)$$

with the current vector $i_{Nj} = \delta_{jk} I_{\mathrm{stim}}$, that corresponds to presenting a stimulation current on the kth electrode. This leads to the currents along each branch

$$\boldsymbol{i}_{\mathrm{sol}} = \mathbf{Y}_{\mathrm{sol}} \cdot (\boldsymbol{v}_N \cdot \mathbf{A}). \qquad (11)$$

A coarse estimation of the longitudinal resistances can be obtained from the resistance of a cylindrical volume of perilymph:

$$R_l = \rho_{\mathrm{peri}} \frac{d}{A_{\mathrm{ST}}} = 446 \,\Omega, \qquad (12)$$

using an electrode spacing $d = 2$ mm and a cross-sectional area of of the scala tympani $A_{\mathrm{ST}} = \pi(1 \text{ mm})^2$. As the spline extrapolation predicts tissue resistances on the order of 1 kΩ to 2 kΩ, the magnitude of transverse resistors can be expected to be significantly larger than R_l.

The model can be solved using an iterative solver to find resistances of the network links $\boldsymbol{r}_{\mathrm{sol}}$ that minimizes

$$\| (\mathbf{Z}_{\mathrm{meas}} - \mathbf{Z}_N) * \mathbf{M}_{\mathrm{mask}} \|, \qquad (13)$$

with the masking matrix $\mathbf{M}_{\mathrm{mask}}$ containing the entries $m_{ij} = 1 - \delta_{ij}$, which excludes the contribution of diagonal matrix elements. The algorithm was implemented in python using a sequential least squares programming method minimizing the Frobenius matrix norm.

For uniformly distributed data points digitized with a quantization step-size 2 s, the mean squared difference between a data point and its quantized value is

$$\frac{1}{s} \int_0^s x^2 dx = \frac{s^2}{3}, \qquad (14)$$

yielding a lower bound that can be expected for an optimal solution

$$s\sqrt{\frac{N(N-1)}{3}} \approx 250 \,\Omega. \qquad (15)$$

There is a large set of $\boldsymbol{r}_{\mathrm{sol}}$ that minimize equation 13 to the same degree. This is not unexpected, and arises from the fact that longitudinal resistors in the network are about two orders of magnitude smaller than transverse resistors. Due to this, networks with strongly varying transverse resistors can still lead to smooth solutions, as very high transverse resistors can be compensated by slight variations in its neighboring nodes. However, the transverse resistors represent the return path through a large volume of biological tissue over a distance of about 30 mm with charge injection points spaced by only a few millimetres. Therefore, they can not be fully decoupled, especially for close nodes, and fluctuating solutions do not well represent the physical reality. In order to prevent the solver from converging to nonphysical, fluctuating solutions, we constrain the arithmetic mean of jumps between neighboring nodes

$$\sqrt{\frac{1}{N-1} \sum_{i=1}^{N-1} (R_i - R_{i+1})^2} \leq 0.5 \cdot \bar{R}, \qquad (16)$$
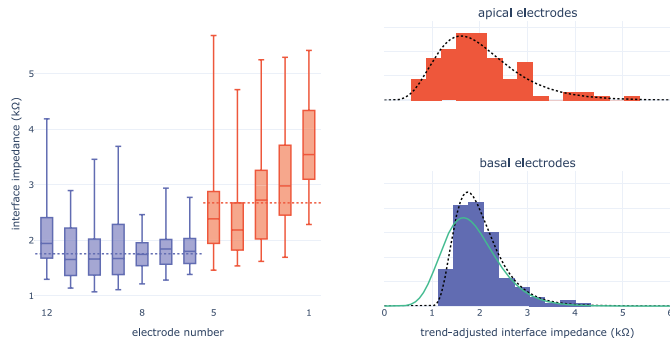
Fig. 6. Distribution of interface impedances Z_i per electrode channel (left) and histogram of the distributions of apical and basal channels after subtraction of the median per channel (right). Fits to log-normal density functions (black, dashed) and the basal distribution estimated from apical data (green) are shown as well.

Fig. 7. Measured electrode resistance versus the angular insertion depth.

separately for transverse, longitudinal and higher order resistances with respect to the arithmethic mean of these resistances $\bar{R}$. Finally, the solution space was probed with a basin-hopping algorithm, that performs random perturbations on the solution vector and accepts solutions stochastically, even if they perform worse than previous solutions. This essentially allows to break free from local minima.

During this process, all minima were stored and from all solutions that optimized (13) to within 3% of the global minimum, the smoothest according to (16) was selected for the following analysis.

III. RESULTS

A. Interface Impedance Distribution

According to (1), subtracting the tissue resistance R_t from the clinical impedance Z_e gives an estimation of the interface impedance Z_i. The values are shown in Fig. 6 (left), grouped by electrode number. Note that the impedances are measured at the end of a charge-balanced pulse. Thus, the contribution of the polarization impedance Z_p is small and these values mainly capture the local bulk resistance R_b.

Average values increase towards the apex. This is consistent with reduced perilymph volume [31] leading to a higher current density and an increase in the local bulk resistance R_b. Additionally, impedances of apical, single pad electrodes are distributed wider than those of basal electrodes.

This difference can be explained by the parallel connection of pairs of basal electrode pads to form a single channel. Basal and apical electrode pads have identical construction except for the doubled surface area of the latter (c.f. Section II-D). Therefore, a simple estimation of the interface impedance distribution of single basal contact pads can be obtained by scaling the distribution of apical contacts by a factor of two. In other words,

$$Z_{\text{basal}} = \frac{(2Z_{\text{apical}})(2Z'_{\text{apical}})}{2Z_{\text{apical}} + 2Z'_{\text{apical}}} = \frac{2Z_{\text{apical}} Z'_{\text{apical}}}{Z_{\text{apical}} + Z'_{\text{apical}}} \quad (17)$$

should follow the distribution of basal electrodes, if Z_{apical} and Z'_{apical} are sampled from the apical distribution.
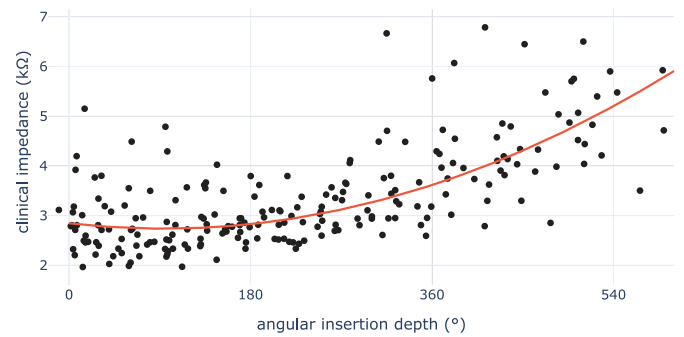
Not included in this reasoning are contributions to the interface impedance caused by reduced perilymph volume, as these vary with the insertion depth and are thus associated with the channel number. The impedance distributions without such contributions can be roughly estimated by removing the median values per channel. Fig. 6 (right) shows these trend-adjusted distributions separately for basal and apical channels. The standard deviation is 881 Ω for apical and 532 Ω for basal electrodes.

The resulting distribution of basal interface impedances computed from the apical distribution according to (17) is overlaid in Fig. 6 (bottom right, green) and shows acceptable agreement with the measured distribution.

B. Clinical Impedances

Clinical impedances correlate significantly with the angular position of the electrodes (Fig. 7). One single recording (11923 Ω) was much higher than all remaining values (below 6960 Ω). It is considered to be an outlier and removed from the data set for further analysis, resulting in a Spearman's correlation coefficient $r = 0.61$ ($p < 0.001$).

The measurements follow approximately a log-normal distribution (c.f. Section III-A). Therefore, least squares regression can be performed on the measurements after transforming data points with $S_i = \log(R_i)$ and imposing different weights for basal and apical electrodes conforming to the ratio of the width of their distributions. A fitted quadratic polynomial is shown in Fig. 7.

C. Influence of Insertion Depth on Tissue Resistance

Fig. 5 (left) shows the tissue resistance, estimated using bivariate spline extrapolation of the telemetry data (c.f. Section II-G) as a function of linear insertion depth. Predominantly, resistance increases with deeper positions inside the cochlea. This suggests that the bulk of the current flows along the cochlea and exits at the basal end, as found previously [11], [32].

Mean and standard deviation of the tissue resistances differ significantly in-between subjects, which can be expected due to anatomical variations. However, there is a significant correlation between those values (Pearson's correlation coefficient $r = 0.80$, $p < 0.001$). This allows to suppress variability between subjects for further analysis by normalizing the resistances by
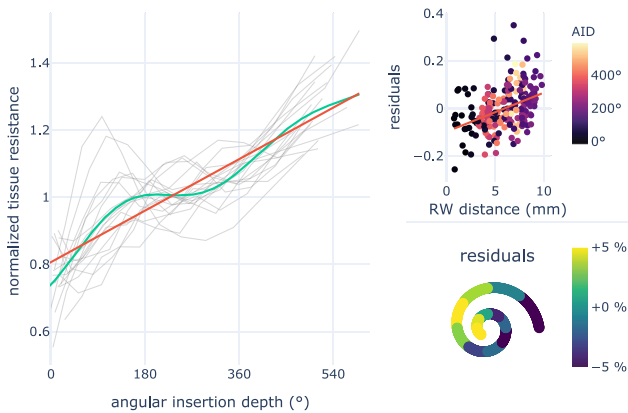
Fig. 8. Normalized tissue resistances as function of the angular position (left) with superimposed fit of a linear (red) and sine-wave modulated function (green). The residuals of the linear fit correlate with the electrode distance to the round window (top right), which can also be observed from the average residuals along the cochlea in bins of 45° (bottom right).

Fig. 9. Error of the linear (bottom) and angular (top) insertion depth estimation per subjects (left) and the corresponding histogram (right). Partially inserted subjects are highlighted in red.

their mean value, according to (4). The normalized values do indeed correlate well across patients (Spearman's correlation coefficient $r = 0.79$, $p < 0.001$), Fig. 5 right).

The normalization emphasizes a region of slower increase near the central electrodes, compared to steeper increases in resistances for basal and apical electrodes. Fig. 8 (left) shows the normalized tissue resistances as a function of the angular insertion depth. The wave shaped modulation is associated with the angular position along the cochlea with maxima roughly at one and three half turns and minima at the basal end and at one full turn.

In order to verify that this modulation is no artefact of the data extrapolation, the same analysis was repeated with the first off-diagonal elements of the voltage matrix and revealed comparable results.

Fig. 8 (upper right) shows the residuals of a linear fit as a function of the distance of each electrode to the round window. This measure correlates significantly (Pearson's $r = 0.40$, $p < 0.001$). The same can be observed in Fig. 8 (lower right) where the median tissue resistance per bins of 45° is shown along the cochlea.

Current levels required for suprathreshold stimulation are weakly correlated with modiolar distance [33], which gives incentive to look for a correlation between impedance values and the distance to the modiolus. Due to limitations in image resolution, we were able to evaluate the modiolar distance for 140 electrodes, most of them with angular depths below 300°. A dependent parameter related to modiolar distance is the distance to the lateral wall, which can also be evaluated for apical electrodes. A significant anti-correlation between these two parameters (Pearson's $r = -0.63$, $p < 0.001$) indicates that effects coupled to modiolar distance would also correlate to lateral wall distance. However, neither lateral wall distance nor modiolar distance did show any significant correlation with the residuals (Pearson's $r = -0.02$, $p = 0.80$ and $r = 0.12$, $p = 0.07$, respectively).

D. Estimating Insertion Depth From Tissue Resistances

Linear insertion depths estimated for all patients using the phenomenological method discussed in Section II-H are shown in Fig. 9. The estimation is designed as a leave-one-out cross validation process. For a given subject, the model parameters are computed from the set of all remaining subjects. The model is used to estimate the subject's insertion depth values, which are then compared to the measured position values. Finally, this process is repeated for each subject.

The method results in an average absolute error of 0.76 mm $\pm$ 0.53 mm and a maximum error of 2.38 mm. The data set contains two partially inserted electrode arrays (subject 6 with 3 and subject 10 with 6 extracochlear electrodes). Insertion depth estimation for these patients using the suggested modification are highlighted in red in Fig. 9.

The proposed method for converting linear to angular insertion depths shows acceptable accuracy. Applying the same cross-validation technique as used for the depth estimation shows an average error of the conversion of 9° (standard deviation 9°) and a maximum error of 59°, when including the correction for the cochlear size. This results in an average error of the estimated angular insertion depths of 15° $\pm$ 12° and a maximum error of 70°. The fitting errors are summarized for all patients in Fig. 9.

E. Lumped-Element Model

Fig. 10 shows the distribution of longitudinal and transverse resistances versus the angular insertion depth, obtained from solving the first order lumped-element network (c.f. Section II-J). The transverse resistances of the basal-most electrodes (1.3 kΩ $\pm$ 0.2 kΩ) are much smaller than any other transverse resistance (21 kΩ $\pm$ 19 kΩ). Since the longitudinal resistances are very small (203 Ω $\pm$ 130 Ω), most of the current indeed flows along the cochlea and exits basally.

Vanpoucke *et al.* observed a pronounced mid-cochlear low-impedance current path in four out of five measured patients,
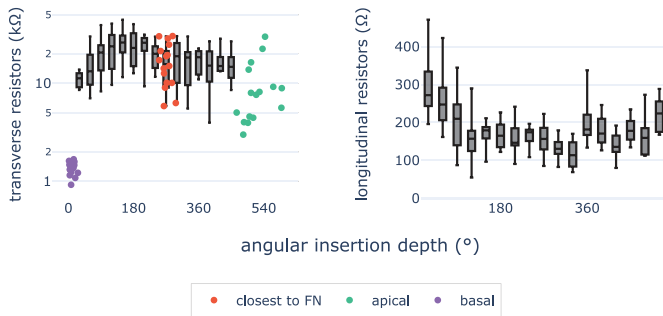
Fig. 10.   Distribution of transverse (left) and longitudinal (right) resistances, computed from the first order lumped-element model. Values of first and last transverse resistances are excluded from the boxplots, as they differ significantly. The channels closest to the facial nerve are superimposed in red.

Fig. 12.   Multiplanar reconstruction of the basal plane of subject 8 and approximate location of the third electrode (white star), where a large portion of the current is drained. The superimposed line shows the orientation of the image plane.
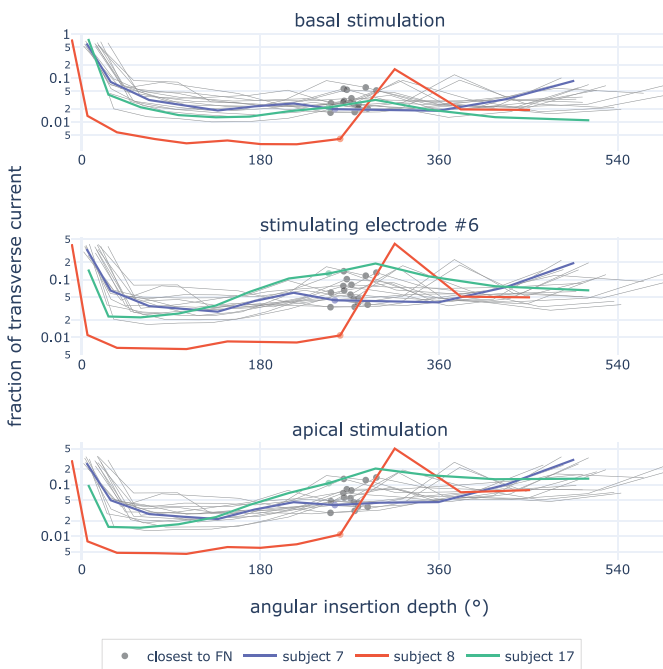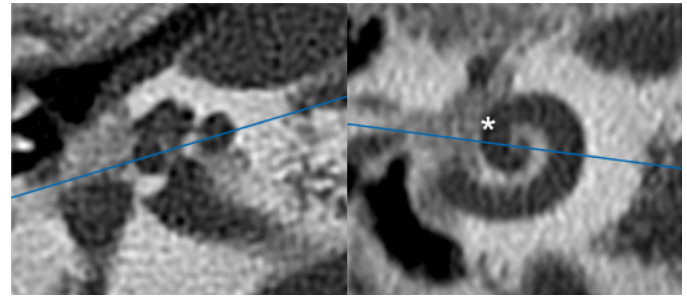

Fig. 11.   Currents along transverse nodes of the first order lumped-element model for basal, medial and apical stimulation as a function of the angular position. Nodes closest to the facial nerve are highlighted by dots.
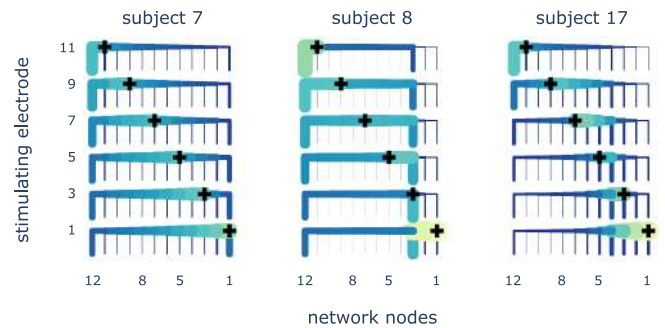

Fig. 13.   Current pathways of the first order lumped-element model for three subjects. Transverse resistors are drawn vertically, the stimulating electrode is marked with a black cross. Width and color scale linearly with current.

which they attributed to current drain through the facial nerve canal [27]. We were not able to observe such a pronounced dip in transverse resistances at the location of the facial nerve in any of our patients. Transverse channels closest to the facial nerve are highlighted in Fig. 10 (left, red markers). Their distribution does not deviate significantly from those of surrounding channel. The same is seen in Fig. 11, which shows the fractions of transverse currents for basal, central and apical stimulation. Locations closest to the facial nerve are highlighted with black markers.

Subject 8 features a low resistive transverse path at around 300°. Medical record revealed that this is a patient with otosclerosis. Fig. 12 shows the corresponding slices of preoperative CT images through the basal plane. In the region of the first cochlear

turn, the radiodensity is significantly lower (988 HU), when compared to other regions adjacent to the cochlea (1882 HU). Reduced radiodensity is correlated with lower bone mineral density [34] which could be a possible explanation for the additional current drain.

Fig. 13 shows the currents along each edge of the network for different stimulation sites and three different subjects. Subject 17 (right) exhibited very high longitudinal resistances in the basal turn, resulting in larger currents towards apical directions for some stimulation sites, which is not the case for any other patient. Subject 7 (left) is an example of regular current paths observed in most patients, where around one third of the current from apical stimulation and about half of the current from basal stimulation returns through the basal return path, with the remaining current leaking uniformly along the cochlea.

IV. DISCUSSION

A. Clinical Impedances

We were able to show a correlation between the measured impedances and insertion depth, confirming our hypothesis (Section III-B). However, a broad distribution of these values is observed, which can be mainly attributed to the interface impedance. In order to deduce intracochlear positions from

telemetry measurements, it is thus favourable to work with tissue resistances estimated from transimpedance data.

B. Interface Impedance Distribution

It is important to keep in mind that the Med-El implants record impedances at the end of the stimulation pulse, when the electrode is in a discharged state. The measurements thus mainly capture the resistive component of the interface impedance R_b, and different recording procedures will influence the contribution of the polarization impedance Z_p.

Interestingly, interface impedances of apical and basal channels differ in the width of their distribution. We suggest that this difference is caused by the parallel connection of pairs of contact pads for basal channels. For certain applications, it is necessary to consider this difference. A simple model, which assumes the same shape of the distribution with doubled values for single basal contact pads, allowed to approximate the basal distribution with acceptable agreement, supporting the proposed explanation.

However, the difference in physical size and different orientations of contact pads within the cochlea are likely to influence the probability of accepting air bubbles on the surface, the speed of foreign body reaction and extend of fibrotic tissue overgrowth. In addition, a trend of increasing interface impedances towards apical channels is not considered in this explanation. Therefore, a complete agreement of this simple relation between apical and basal interface impedance distribution should not be expected.

C. Tissue Resistance

We found that bivariate spline extrapolation of transimpedance recordings is a simple and robust method for estimating tissue resistances. Tissue resistance predominantly increases linearly with insertion depth. In addition to this rise, a modulation corresponding to higher resistances of distal segments of the cochlea with respect to the round window location arises when looking at the normalized tissue resistances of all patients. The effect is rather small and is masked by individual variations for single subjects.

We did not find a significant correlation with the electrode's distance to the modiolus or lateral wall. The correlation between the modulation and angular position within the cochlea, however, does not necessarily imply a causal relation with the physical distance between stimulating and reference electrodes, as variations in tissue conductivity between proximal and distal segments of the cochlea could cause the same correlation.

D. Insertion Depth Estimation From Tissue Resistance

Combined with a purely phenomenological model, this allowed us to estimate linear and angular insertion depths with an accuracy on the order of the spacing between electrodes. These recordings are typically performed during surgery and the process is computationally inexpensive. Since the round window niche is frequently invisible or only partially visible [35], this method may provide intraoperative feedback for assessing implant placement in cases of poor visibility of the cochlear

access. This may in particular apply for surgical procedures using a posterior tympanotomy approach under microscopic supervision.

Electrode migration is a common complication with cochlear implants [36]. Testing electrode placement could be valuable application when coiling of the electrode lead into the mastoidectomy and during wound closure, where visual assessment is no longer possible.

The proposed method does not allow to be directly applied to angular insertion depths. Thus, an additional step of converting the linear estimates to angular values is needed. We have shown that a conversion based on the established correlation between linear and angular insertion depths and the cochlear size [29], [30] gives acceptable accuracy. However, it does still contribute significantly to the resulting errors, especially for apical electrodes where both the accuracy of the conversion declines, and the angular values are more sensitive to inaccuracies due to the reduced cochlear radius.

From technical evaluations [37], [38] the ideal localization errors can be expected to lie in the range of the image voxel size (usually around 0.3 mm). This translates to angular errors of approximately 5° to 10° depending on the cochlear egion. However, we expect an effective clinical error about twice as high (10° to 20°), as few clinics have the specific neuroradiological expertise and algorithms available and usually rely on manual assessment of the electrode positions in planar CT projections [18], [39]. The angular errors presented herein are comparable to clinically obtained angular insertion depth measurements [40].

The two partially inserted electrode arrays have 3 and 6 extracochlear electrodes, which correspond to a distance between the basal-most contact and the round window of 4.4 mm and 10.6 mm, respectively. Both could therefore be visually observed during surgery. For uncertain cases, the method proposed by de Rijk *et al.* [41] could be applied to detect extracochlear electrodes from transimpedance measurements.

While the depth estimations for the partial insertion cases are comparable to the other results, we expect lower precision due to the additional second fitting parameter and the lower number of impedance values contributing to the estimation. This needs verification on a larger number of such cases.

E. Lumped-Element Model

While tissue resistances can also be computed using a lumped-element model, we needed to impose additional constraints to prevent the algorithm from converging to nonphysical solutions. Networks of lower order did not allow to reproduce subtle dependencies such as the positional modulation discussed in Section III-C. It should be noted that the implants in our study have a lower number of electrodes with larger inter-electrode spacing and that the recordings are digitized with lower resolution than in the initial work on the topic by Vanpoucke *et al.* [11]. We think that the coarse digitization of the measured signal is limiting the validity of the modelled resistances.

Modelling the system in terms of longitudinal and transverse resistors has nevertheless proved to be valuable. It allowed to

show apical current drain in one subject with locally reduced bone density.

F. Study Limitations

Due to the limited size of the data set, a cross-validation technique was applied in order to maximise the size of the available training set without biasing the results. The methods established in this work need to be validated in future prospective studies.

The presented work focuses on the analysis of telemetry data measured in an intraoperative setting. Repeated measurements could potentially allow to track the array position during insertion or wound closure. If applicable to postoperative recordings, depth estimations could be utilized for monitoring electrode migration or for patient-specific tonotopic fitting methods without the additional radiation exposure that is associated with medical imaging.

For such applications, it should be considered that cochlear implantation causes foreign body reaction, with increased number of macrophages and fibrous tissue build-up surrounding the electrode [42]. This affects the temporal progression of electrode impedances [43]. High impedance values can also be caused by air bubbles on the electrode contact, which generally dissipate within hours to days after the surgery [8], [10].

Therefore, tissue resistance, interface impedance and current path estimations computed from intraoperative recordings may not be representative of postoperative conditions [44]. Further studies are required for specific validation of the applicability to postoperative telemetry data of the methods presented herein.

Finally, rectangular wave pulses cause components at multiples of the base frequency of the stimulation frequency, where bone and nerve tissue have well documented capacitive effects [24]. While the present analysis is limited to purely resistive behaviour, impedance spectroscopy and impedance waveform recordings might provide additional insight, for example for the analysis of current drain through the facial nerve canal [27].

V. CONCLUSION

In this article, we reviewed the lumped-element model as proposed by Vanpoucke *et al.* [11] with the implants of a different manufacturer. The model allowed to identify high apical current drain in a patient with otosclerosis. Contrary to previous findings [27], we did not observe large current drain through the facial nerve canal.

In addition, we demonstrated correlations between both angular and linear insertion depth with measured clinical impedances and tissue resistances.

We were able to show a difference in the distribution of interface impedances for apical and basal electrodes of the free fitting electrode arrays used in this study, which we suggest is caused by the parallel connection of the basal contact pads.

Correlating the tissue resistance with electrode position allowed to estimate the linear insertion depth of 18 subjects with fully implanted electrode arrays with errors below 2.38 mm and an average absolute error of 0.76 mm. The conversion to angles based on the correlation of linear and angular positions led to

estimates of angular insertion angles with a maximum error of $70°$ and an average absolute error of $15°$.

A potential application of this method could be the verification of electrode placement after implant management, i.e. coiling of the electrode lead into the mastoidectomy and wound closure, where visual assessment is not possible anymore.

REFERENCES

[1] A. A. Eshraghi *et al.*, "The cochlear implant: Historical aspects and future prospects," *Anatomical Rec.: Adv. Integrative Anatomy Evol. Biol.*, vol. 295, no. 11, pp. 1967–1980, Nov. 2012.

[2] F. Heutink *et al.*, "Angular electrode insertion depth and speech perception in adults with a cochlear implant: A systematic review," *Otol. Neurotol.*, pp. 900–910, May 2019.

[3] M. K. Cosetti *et al.*, "An evidence-based algorithm for intraoperative monitoring during cochlear implantation," *Otol. Neurotol.*, vol. 33, no. 2, pp. 169–176, Feb. 2012.

[4] F. B. van der Beek *et al.*, "Intracochlear position of cochlear implants determined using CT scanning versus fitting levels: Higher threshold levels at basal turn," *Audiol. Neurotol.*, vol. 21, no. 1, pp. 54–67, 2016.

[5] Y. Zhaoa *et al.*, "Validation of image-guided cochlear implant programming techniques," 2019, *arXiv:1909.10137*, p. 37.

[6] S. Sipari *et al.*, "The image fusion technique for cochlear implant imaging: A study of its application for different electrode arrays," *Otol. Neurotol.*, pp. e216–e222, Nov. 2019.

[7] W. Wimmer *et al.*, "Cone beam and micro-computed tomography validation of manual array insertion for minimally invasive cochlear implantation," *Audiol. Neurotol.*, vol. 19, no. 1, pp. 22–30, 2014.

[8] J. L. Goehring *et al.*, "How well do cochlear implant intraoperative impedance measures predict postoperative electrode function?" *Otol. Neurotol.*, vol. 34, no. 2, pp. 239–244, Feb. 2013.

[9] Q. Mesnildrey *et al.*, "Impedance measures for a better understanding of the electrical stimulation of the inner ear," *J. Neural Eng.*, vol. 16, no. 1, Feb. 2019, Art. no. 016023.

[10] "Mi1250 synchrony 2 surgical guide," 2019.

[11] F. Vanpoucke, A. Zarowski, and S. Peeters, "Identification of the impedance model of an implanted cochlear prosthesis from intracochlear potential measurements," *IEEE Trans. Biomed. Eng.*, vol. 51, no. 12, pp. 2174–2183, Dec. 2004.

[12] F. J. Vanpoucke, P. B. Boermans, and J. H. Frijns, "Assessing the placement of a cochlear electrode array by multidimensional scaling," *IEEE Trans. Biomed. Eng.*, vol. 59, no. 2, pp. 307–310, Feb. 2012.

[13] M. G. Zuniga *et al.*, "Tip fold-over in cochlear implantation: Case series," *Otol. Neurotol.*, vol. 38, no. 2, pp. 199–206, Feb. 2017.

[14] C.-T. Tan *et al.*, "Real-time measurement of electrode impedance during intracochlear electrode insertion: Real-Time intracochlear electrode impedance," *Laryngoscope*, vol. 123, no. 4, pp. 1028–1032, Apr. 2013.

[15] C. K. Giardina *et al.*, "Impedance measures during in vitro cochlear implantation predict array positioning," *IEEE Trans. Biomed. Eng.*, vol. 65, no. 2, pp. 327–335, Feb. 2018.

[16] C. Zierhofer, I. Hochmair, and E. Hochmair, "The advanced combi 40+ cochlear implant," *Amer. J. Otol.*, vol. 18, no. 6, pp. S37–S38, 1997.

[17] A. P. Sanderson *et al.*, "Exploiting routine clinical measures to inform strategies for better hearing performance in cochlear implant users," *Frontiers Neurosci.*, vol. 12, Jan. 2019, Art. no. 1048.

[18] B. M. Verbist *et al.*, "Consensus panel on a cochlear coordinate system applicable in histologic, physiologic, and radiologic studies of the human cochlea," *Otol. Neurotol.*, vol. 31, no. 5, pp. 722–730, Jul. 2010.

[19] W. Wimmer *et al.*, "Robust cochlear modiolar axis detection in CT," in *Medical Image Computing and Computer Assisted Intervention – MICCAI 2019*, D. Shen *et al.*, Eds. Berlin, Germany: Springer, 2019, vol. 11768, pp. 3–10.

[20] M. Tykocinski, L. T. Cohen, and R. S. Cowan, "Measurement and analysis of access resistance and polarization impedance in cochlear implant recipients," *Otol. Neurotol.*, vol. 26, no. 5, pp. 948–956, Sep. 2005.

[21] B. Swanson, P. Seligman, and P. Carter, "Impedance measurement of the Nucleus 22-electrode array in patients," *Ann. Otol., Rhinol. Laryngol.*, pp. 141–144, 1995.

[22] Y. Henkin *et al.*, "Changes over time in electrical stimulation levels and electrode impedance values in children using the Nucleus 24M cochlear implant," *Int. J. Pediatric Otorhinolaryngol.*, vol. 67, no. 8, pp. 873–880, Aug. 2003.

[23] Y. Henkin *et al.*, "A longitudinal study of electrical stimulation levels and electrode impedance in children using the Clarion cochlear implant," *Acta Oto-Laryngologica*, vol. 126, no. 6, pp. 581–586, Jan. 2006.

[24] C. Inguva *et al.*, "Frequency-dependent simulation of volume conduction in a linear model of the implanted cochlea," in *Proc. 7th Int. IEEE/EMBS Conf. Neural Eng. (NER)*, Apr. 2015, pp. 426–429.

[25] S. Bai *et al.*, "Electrical stimulation in the human cochlea: A computational study based on high-resolution micro-CT scans," *Frontiers Neurosci.*, vol. 13, Dec. 2019, Art. no. 1312.

[26] C. van den Honert and D. C. Kelsall, "Focused intracochlear electric stimulation with phased array channels," *J. Acoust. Soc. Amer.*, vol. 121, no. 6, 2007, Art. no. 3703.

[27] F. Vanpoucke *et al.*, "The facial nerve canal: An important cochlear conduction path revealed by clarion electrical field imaging," *Otol. Neurotol.*, vol. 25, no. 3, pp. 282–289, May 2004.

[28] C. Rathgeb *et al.*, "Clinical applicability of a preoperative angular insertion depth prediction method for cochlear implantation," *Otol. Neurotol.*, vol. 40, no. 8, pp. 1011–1017, Sep. 2019.

[29] L. Anschuetz *et al.*, "Cochlear implant insertion depth prediction: A temporal bone accuracy study," *Otol. Neurotol.*, pp. e996–e1001, 2018.

[30] B. Escudé *et al.*, "The size of the cochlea and predictions of insertion depth angles for cochlear implant electrodes," *Audiol. Neurotol.*, vol. 11, no. 1, pp. 27–33, 2006.

[31] S. Biedron *et al.*, "The internal dimensions of the cochlear scalae with special reference to cochlear electrode insertion trauma," *Otol. Neurotol.*, vol. 31, no. 5, pp. 731–737, Jul. 2010.

[32] L. H. M. Mens, "Advances in cochlear implant telemetry: Evoked neural responses, electrical field imaging, and technical integrity," *Trends Amplification*, vol. 11, no. 3, pp. 143–159, Sep. 2007.

[33] T. J. Davis *et al.*, "Relationship between electrode-to-modiolus distance and current levels for adults with cochlear implants," *Otol. Neurotol.*, vol. 37, no. 1, pp. 31–37, Jan. 2016.

[34] J. J. Schreiber, P. A. Anderson, and W. K. Hsu, "Use of computed tomography for assessing bone mineral density," *Neurosurgical Focus*, vol. 37, no. 1, Jul. 2014.

[35] A. Kashio *et al.*, "Predicting round window niche visibility via the facial recess using high-resolution computed tomography," *Otol. Neurotol.*, pp. e18–e23, Oct. 2014.

[36] A. Ishiyama, F. Risi, and P. Boyd, "Potential insertion complications with cochlear implant electrodes," *Cochlear Implants Int.*, vol. 21, no. 4, pp. 1–14, Feb. 2020.

[37] Y. Zhao *et al.*, "Validation of cochlear implant electrode localization techniques," *Proc. SPIE*, Mar. 2018.

[38] H. J. Theunisse *et al.*, "Cone-beam CT versus multi-slice CT systems for postoperative imaging of cochlear implantation – A phantom study on image quality and radiation exposure using human temporal bones," *Otol. Neurotol.*, vol. 36, no. 4, pp. 592–599, 2015.

[39] R. Harris *et al.*, "A practical, single-view alternative to Stenver's for plain radiographic unilateral and bilateral post-cochlear implant position check," *Cochlear Implants Int.*, vol. 12, no. 1, pp. 53–56, Feb. 2011.

[40] N. W. Todd and T. I. Ball, "Interobserver agreement of coiling of Med-El cochlear implant: Plain X-ray studies," *Otol. Neurotol.*, vol. 25, no. 3, pp. 271–274, May 2004.

[41] S. R. de Rijk *et al.*, "Detection of extracochlear electrodes in cochlear implants with electric field imaging/transimpedance measurements: A human cadaver study," *Ear Hearing*, 2020. [Online]. Available: https://journals.lww.com/ear-hearing/Abstract/publishahead/Detection_of_Extracochlear_Electrodes_in_Cochlear.98713.aspx

[42] T. Okayasu *et al.*, "The distribution and prevalence of macrophages in the cochlea following cochlear implantation in the human: An immunohistochemical study using anti-iba1 antibody," *Otol. Neurotol.*, pp. e304–e316, Nov. 2019.

[43] D. P.-Y. Lin *et al.*, "Differences in the impedance of cochlear implant devices within 24 hours of their implantation," *PloS One*, vol. 14, no. 9, Sep. 2019, Art. no. e0222711.

[44] A. M. El Shennawy *et al.*, "Telemetry changes over time in cochlear implant patients," *Hearing, Balance Commun.*, vol. 13, no. 1, pp. 24–31, Jan. 2015.